

Room-Temperature Crystallization of Ultralong (≈ 3.5 mm) CsCu_2I_3 Microbelt to Suppress Carrier Recombination for High-Performance UV Heterojunction Photodetector

Ziqing Li, Chaolei Zuo, Xinya Liu, Zhuangzhuang Ma, Zhifeng Shi,* and Xiaosheng Fang*

Lead-free ternary copper iodide perovskite analogues demonstrate great potential in photodetector, due to their nontoxicity and excellent photophysical properties. However, the fast carrier recombination limits the photoelectric conversion efficiency. Herein, a room-temperature growth strategy with the selected raw ratio is adopted to enhance carrier dynamics. The optimized-grown CsCu_2I_3 single crystal exhibits longer carrier lifetime of 157 ns, and its switch ratio and response time are enhanced by 20 000% and 600% compared with those of stoichiometric-grown single crystal, respectively. Furthermore, space-confined method is introduced to prepare ultralong single-crystalline CsCu_2I_3 microbelt, with the aspect ratio up to 600. The sensitivity and self-powered performance of the UV photodetector are improved through constructing heterojunction with p-CuI and asymmetric electrodes. The enhanced performance is ascribed to superior type-II band alignment between CsCu_2I_3 and CuI, which effectively promotes the separation of photo-generated carriers. This work not only provides an efficient way to boost the photoresponse in low-dimensional metal halide perovskite analogue, but also displays 1D anisotropic growth for potential application in large-area vapor-assisted patterned devices.

has surpassed 25.5%,^[2] and the external quantum efficiency (EQE) of perovskite LEDs has been dramatically boosted to over 20%.^[3] However, there exist two main problems with organic lead halide perovskites. First, the toxicity of lead in perovskite has severely restricted its commercialization. Therefore, on the basis of inheriting the excellent performance of lead-based perovskites, it is of great significance to develop nontoxic lead-free halide perovskites for optoelectronic applications.^[4] To date, a rapid development has been achieved in the past years, and a large amount of environment-friendly metal cations have been selected to replace Pb^{2+} to reduce the toxicity to humans and the environment, including Sn^{2+} , Cu^+ , Bi^{3+} , Ge^{2+} , and Sb^{3+} .^[2] Second, the instability to moisture, light and heat, which comes from the intrinsic organic cationic group, limits its practical application.^[4] From the application point of view, it is required that the lead-free halide perovskite should

1. Introduction

Organic lead halide perovskite has been widely studied in the fields of solar cells, photodetectors, light-emitting diodes (LEDs), lasers, and memories.^[1] A significant breakthrough has been witnessed in developing high-performance perovskite optoelectronic devices in the past years. For instance, the current certified power conversion efficiency of perovskite solar cells

exhibit enough stability to the disturbance from external environment. It is proved that reducing the structural dimensions of the perovskite can effectively improve its stability.^[5] Consequently, low-dimensional metal halide perovskite analogues at molecular level, which demonstrate good stability and unique photophysical properties, have attracted tremendous attention in the field of optoelectronics.^[6]

Recently, as an ideal candidate of novel low-dimensional metal halide perovskite analogues, 1D CsCu_2I_3 has been investigated in many aspects of photodetection field. Highly stable CsCu_2I_3 single crystal was fabricated as facet-dependent, fast response, and broadband photodetector.^[7] Oriented-structured CsCu_2I_3 film detector achieved high-resolution X-ray imaging.^[8] Solution-processed CsCu_2I_3 nanowires were introduced to construct polarization-sensitive and flexible UV photodetector.^[9] High-performance deep UV photodetector was built up based on the CsCu_2I_3 film.^[10] In addition, 1D CsCu_2I_3 perovskite analogue also shows great potential in the field of LEDs. Highly efficient 1D CsCu_2I_3 single crystal was emerged as the down-conversion phosphors for white-LEDs.^[11] Through localized 1D excitonic recombination, a high photoluminescence quantum yield (PLQY) was realized in CsCu_2I_3 single crystal.^[12] However, this typical strong excitonic recombination and short carrier

Z. Q. Li, C. L. Zuo, X. Y. Liu, X. S. Fang
Department of Materials Science
Institute of Optoelectronics
Fudan University
Shanghai 200433, P. R. China
E-mail: xshfang@fudan.edu.cn

Z. Z. Ma, Z. F. Shi
Key Laboratory of Materials Physics of Ministry of Education
School of Physics and Microelectronics
Zhengzhou University
Daxue Road 75, Zhengzhou 450052, P. R. China
E-mail: shizf@zzu.edu.cn

 The ORCID identification number(s) for the author(s) of this article can be found under <https://doi.org/10.1002/adom.202102315>.

DOI: 10.1002/adom.202102315

lifetime largely restrict the separation of photogenerated electrons and holes, limiting the photoelectric conversion efficiency of CsCu₂I₃ single crystal and bringing great challenges to the application in photoelectric conversion devices.^[2] In general, fewer defects contribute to a longer carrier lifetime, and therefore high-quality single crystal with lower surface trap density is beneficial to the development of perovskite analogue semiconductors.^[7] Moreover, other strategies have been introduced to facilitate the photoelectric conversion efficiency, including modifying molecular structure and constructing heterojunction interface.^[13]

To date, a series of patterning technologies, which can generate and confine photons or carriers transport along regulated orientation, have been applied in perovskites to realize nano/microstructured thickness or surface to further improve the device performances in the integrated circuits.^[14] Compared with the perovskite thin film, 1D perovskite micro/nanostructure demonstrates peculiar advantage for device applications.^[15] In particular, controlled growth of ultralong perovskite wire is important for both fundamental research and practical application, such as flexible electronics, large-area production and patterning technology.^[16] At present, a large amount of strategies have been adopted to develop 1D metal halide perovskite nanowire, nanobelt, microwire, and microbelt, including template-assisted growth, chemical vapor deposition and solution process.^[14] It is well known that the space-confined solution method is an effective and low-cost process to reduce the film thickness. Horizontal MAPbBr₃ nanowire arrays have been successfully fabricated through PDMS space-confined solution growth.^[14] Vertical MAPbI₃ nanowire arrays have been grown by template-assisted space-confined growth.^[14] With the assists of antisolvent and confined space, monocrystalline CsPbBr₃ microwire arrays could also be constructed.^[14] A simple blade coating method was applied in the lateral growth of 1D single-crystalline MAPbI₃ microwire arrays.^[14] To a certain extent, metal halide perovskite analogue arrays have completely changed many fields of optoelectronics owing to their potential in fabricating multifunctional and large-scale integrated devices.

In this work, a general space-confined growth method is adopted to develop ultralong single-crystalline 1D CsCu₂I₃ microbelt with the aspect ratio up to 600, based on a room-temperature (RT) growth strategy. Generally, the selected raw ratio is introduced to grown high-quality and transparent single crystals, which suppress carrier recombination. For optimized-grown CsCu₂I₃ single crystal, prolonged carrier lifetime promotes the switch ratio up to 600 and reduces the response time to 40 μs, with 20 000% and 600% enhancement compared with those of stoichiometric-grown single crystal, respectively. Furthermore, through constructing heterojunction with p-CuI and asymmetric electrodes, the responsivity and self-powered performance of the UV photodetector are greatly improved. The enhanced performance is associated with the effective separation of photogenerated carriers, resulted from type-II band alignment between CsCu₂I₃ and p-CuI. This work not only introduces a strategy of extending carrier lifetime on low-dimensional metal halide perovskite analogue, but also demonstrates the future prospects for the development of device architectures based on patterning technology.

2. Results and Discussion

It is well known that the single crystal grown at lower temperature has a lower bulk defect density, thus assisting to strengthen the optoelectronic quality.^[17] Ternary copper iodide single crystals are successfully grown through low-cost antisolvent vapor assisted method under RT. **Figure 1a** shows the schematic diagram of the whole synthesis process. The initial raw materials CsI and CuI are dissolved in mixed solvent DMSO/DMF to obtain a clear saturated solution. As shown in Figure S1 in the Supporting Information, the color of the precursor solution changes from light to dark with the increase of CuI at the stirring stage, and CuI precipitation is observed obviously for raw material ratio ($[\text{CuI}]/([\text{CuI}] + [\text{CsI}])$) of 80%. At the end of growth process, the transparent, high-quality CsCu₂I₃ and Cs₃Cu₂I₅ single crystals are obtained by isopropanol (IPA) rinsing for raw material ratio of 20%, 40%, and 50%, while light-green CsCu₂I₃ single crystals are obtained for stoichiometric growth (66.6%) and no crystals are obtained for excessive CuI contents (80%). As shown in Figure 1b, with the raw material ratio changing from 20% to 66.6%, large amounts of the as-grown single crystals are acquired, and the obvious phase evolution is supported by evident blue (Cs₃Cu₂I₅) and yellow (CsCu₂I₃) photoluminescence emission under ultraviolet (UV) illumination, respectively. As we can see from Figure 1c, with the raw material ratio changing from 20% to 66.6%, it is confirmed that the peak position and intensity of X-ray diffraction (XRD) patterns are in good agreement with the standard card from the orthorhombic Cs₃Cu₂I₅ (PDF#01-072-9850, Pnma) to the orthorhombic CsCu₂I₃ (PDF#01-072-9857, Cmcm). The structural information of the phase evolutions is summarized in Table S1 in the Supporting Information in detail, where the lattice parameters are obtained by XRD refinement. It is inferred that the raw material ratio of 50% is suitable for optimized growth of CsCu₂I₃ single crystal, compared with the stoichiometric-grown single crystal (66.6%). This can be attributed to the excessive CsI inhibiting the precipitation of CuI, thereby improving the crystalline quality of the single crystal. As shown in Figure S8 in the Supporting Information, high-resolution XPS patterns of Cs 3d, Cu 2p, I 3d core levels are further to confirm the chemical composition of CsCu₂I₃ single crystals prepared with 50% raw ratio. The element ratio of Cs:Cu:I is calculated to be 5.19:9.26:13.52, which is close to the nominal ratio of CsCu₂I₃.

Photoelectric measurement is further conducted to compare the photoelectric performance of stoichiometric-grown and optimized-grown CsCu₂I₃ millimeter rod single crystals. As shown in **Figure 2a,d**, the optimized growth brings transparent and colorless single crystal with length up to 5 mm, while the stoichiometric growth results in light-green single crystals with contaminated surfaces. **Figure 2b** demonstrates the enhanced static photoelectric performance in optimized-grown CsCu₂I₃ millimeter rod single crystal. **Figure 2c** further displays the enhanced switch ratio for optimized-grown CsCu₂I₃ millimeter rod single crystal. For stoichiometric-grown CsCu₂I₃ single crystal, the prepared photodetector displays a lower dark current at the initial time, and then reaches a steady higher dark current for subsequent on-off cycles. It is worth mentioning that the photocurrent is improved and the switch ratio is enhanced by 20 times, which is mainly due to the fewer surface defects

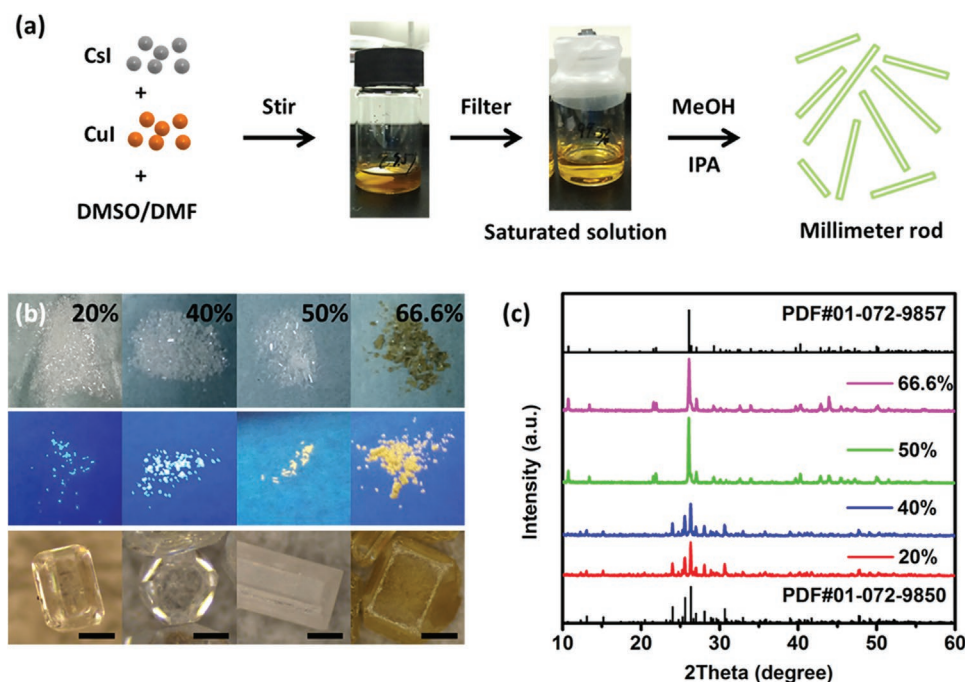


Figure 1. Optimized growth process of ternary copper iodide single crystals. a) Schematic diagram of the synthesis process. b) Phase evolution with changes in raw material ratio. Top: the photographs of as-grown crystals. Middle: the photographs of as-grown crystals under UV illumination. Bottom: the enlarged optical photographs of as-grown crystals. The scale bar is 100 μm . c) Powder X-ray diffraction pattern of the as-grown single crystals prepared with different raw ratios.

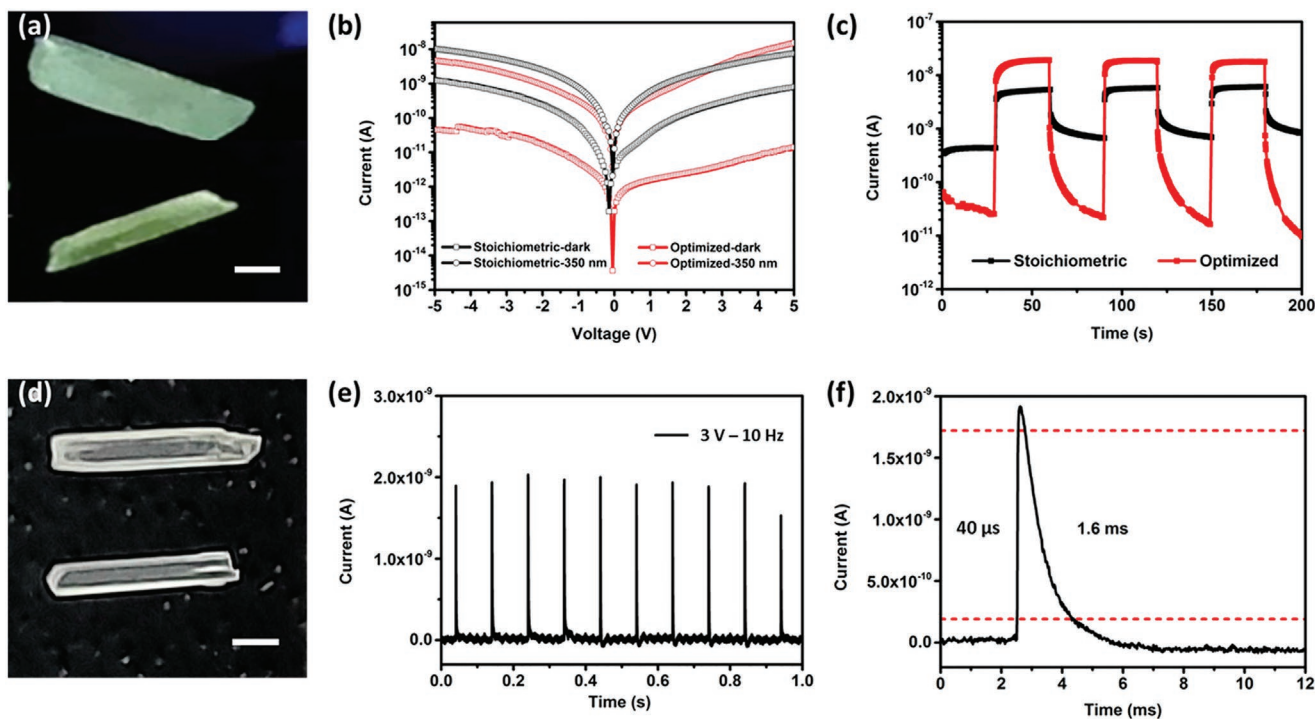


Figure 2. Enhanced photoelectric performance of CsCu_2I_3 millimeter rod single crystal. a) Photograph of the millimeter rod with stoichiometric growth. The scale bar is 1 mm. b) I - V curves for millimeter rods with stoichiometric and optimized growth, respectively. c) I - t curves for millimeter rods with stoichiometric and optimized growth, respectively. d) Photograph of the millimeter rod with optimized growth. The scale bar is 1 mm. e) Photoresponse to 355 nm pulse laser with a modulation frequency of 10 Hz at 3 V bias. f) Calculated rise and decay time from single pulse response curve.

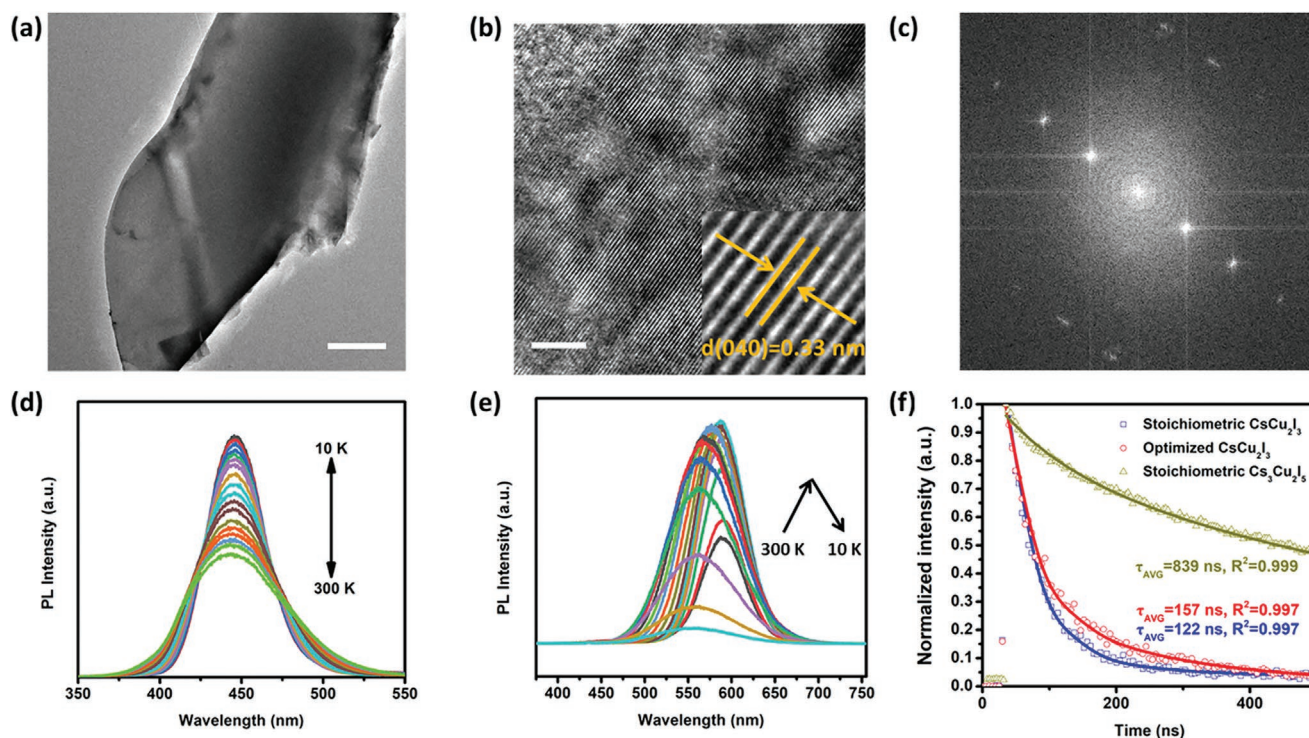


Figure 3. a) Low-resolution TEM image of CsCu_2I_3 prepared by ultrasonic treatment from bulk crystals. The scale bar is 1 μm . b) High-resolution TEM image of CsCu_2I_3 , and the inset is the enlarged section. The scale bar is 5 nm. c) The corresponding fast Fourier transform (FFT) image of CsCu_2I_3 . d) Temperature-dependent PL spectra of $\text{Cs}_3\text{Cu}_2\text{I}_5$ single crystal at the temperature range of 10–300 K. e) Temperature-dependent PL spectra of CsCu_2I_3 single crystal at the temperature of 10–300 K. f) Time-resolved PL decay and fitting curve for stoichiometric CsCu_2I_3 , optimized CsCu_2I_3 and stoichiometric $\text{Cs}_3\text{Cu}_2\text{I}_5$.

in optimized-grown CsCu_2I_3 single crystal. Figure 2e shows the transient response time of the optimized-grown CsCu_2I_3 millimeter rod single crystal. Under 355 nm laser pulse illumination, the device demonstrates steady, rapid and repeatable photoresponse with sharp pulse signal at 3 V bias voltage. The time-resolved photoresponse of a single pulse is clearly shown in Figure 2f. The rise time defined as 10% to 90% is obtained to be 40 μs , the decay time defined as 90% to 10% is estimated to be 1.6 ms. Notably, the decay time is shortened by at least an order of magnitude compared with other reports, as shown in Table 2. It is concluded that the optimized-grown CsCu_2I_3 single crystal shows higher photocurrent, higher switch ratio and faster response speed than stoichiometric-grown CsCu_2I_3 single crystal, which may benefit from the low-temperature growth strategy and selected raw material ratio.

As shown in Figure 3a, a piece of CsCu_2I_3 with several microns, which is prepared by ultrasonic treatment from bulk single crystal, can be clearly seen in the low-resolution TEM image. Figure 3b demonstrates high-resolution TEM image of CsCu_2I_3 , and the inset shows visible crystal lattice fringe with lattice spacing of 0.33 nm, which is corresponding to (040) crystal plane of CsCu_2I_3 . Figure 3c exhibits the corresponding fast Fourier transform (FFT) image of CsCu_2I_3 , which further confirm the single crystal structure. As shown in Figure 3e, with the temperature increasing from 10 to 300 K, the strong thermal quenching is observed due to heat-induced carrier nonradiative recombination.^[18] It can be more clearly seen in Figure S2b in the Supporting Information that the PL peak position demonstrates

a successive blue-shift with rising temperature, however, the PL intensity first rises and subsequently falls with the temperature increasing. The maximum peak intensity locates at the temperature of 80 K, and this indicates that there may exist a phase transition for CsCu_2I_3 single crystal at low temperature.^[19] As shown in Figure 3d, with the temperature increasing from 10 to 300 K, the PL intensity of $\text{Cs}_3\text{Cu}_2\text{I}_5$ single crystal is accordingly decreasing because of the strong thermal quenching phenomenon and thermally enabled nonradiative recombination.^[3] The similar spectral shape and peak position under different temperature indicate that this broadband emission roots from the same excited state relaxation. As shown in Figure S2a in the Supporting Information, the slight asymmetric spectral shape is ascribed to multiple self-trapped emissions in $\text{Cs}_3\text{Cu}_2\text{I}_5$ single crystal,^[20] which are located at 445 and 499 nm, respectively.

As shown in Figure 3f, the suppressed carrier recombination is confirmed by the extended carrier lifetime, which is fitted to be 839, 157, and 122 ns for sample 40%, sample 50%, and sample 66.6%, according to the biexponential function^[21–22]

$$I(t) = A_1 e^{-\frac{t}{\tau_1}} + A_2 e^{-\frac{t}{\tau_2}} \quad (1)$$

$$\tau = \frac{A_1 \tau_1^2 + A_2 \tau_2^2}{A_1 \tau_1 + A_2 \tau_2} \quad (2)$$

where A_1 and A_2 are weighted factors for the two exponential components, τ_1 and τ_2 are corresponding lifetimes. Compared to that of stoichiometric-grown CsCu_2I_3 (66.6%), the longer

Table 1. PL Lifetime parameters of the ternary copper iodide perovskite analogues.

Material		Lifetime τ_{AVG} [ns]	Refs.
CsCu ₂ I ₃	Single crystal	157	This work
	Single crystal	63.6	[12]
	Single crystal	–	[25]
	Polycrystalline film	40.6	[3]
	Polycrystalline film	149	[26]
Cs ₃ Cu ₂ I ₅	Single crystal	839	This work
	Single crystal	–	[27]
	Single crystal	464	[28]
	Single crystal	997.41	[25]
	Nanocrystal	–	[24]

carrier lifetime of optimized-grown CsCu₂I₃ (50%) confirms that suppressed carrier recombination are observed to facilitate carrier separation,^[23] which explains the enhanced photoelectric properties in optimized-grown CsCu₂I₃ single crystal. The obtained lifetimes are comparable to those in literatures, as summarized in Table 1. By fitting the temperature-dependent full-width at half-maximum (FWHM) curve, the Huang–Rhys factor (S) and phonon frequency ($h\omega_{\text{phonon}}$) can be extracted from the following equation^[3,24]

$$FWHM(T) = 2.36 \sqrt{S} h\omega_{\text{phonon}} \sqrt{\coth \frac{h\omega_{\text{phonon}}}{2\kappa T}} \quad (3)$$

As shown in Figure S3 in the Supporting Information, the Huang–Rhys factor (S) is fitted to be 37.0 and 45.8 for Cs₃Cu₂I₅ and CsCu₂I₃ single crystals, respectively. The values of phonon frequency ($h\omega_{\text{phonon}}$) are 18.2 and 12.7 meV for Cs₃Cu₂I₅ and CsCu₂I₃ single crystals, respectively. It is noted that the S factors are much higher than those of other materials with the band-edge photoluminescence characteristics. This indicates that there is strong electron–phonon coupling in ternary copper iodides, which assists to form self-trapped emissions below bandgap.^[24] It is reasonable to infer that the RT growth strategy with the selected raw material ratio can effectively inhibit carrier recombination, thereby enhancing the photoelectric property for ternary copper iodide single crystals.

To further boost the photoelectric performance of CsCu₂I₃-based photodetector, p-CuI is utilized for constructing the heterojunction accompanied by asymmetric electrodes, considering appropriate type-II band alignment.^[29] As shown in Figure S6 in the Supporting Information, the as-prepared CuI thin film is dense and free of pin holes, with the particle size of several hundred nanometers. As shown in Figure S7 in the Supporting Information, the intensity and position of the XRD peaks are well-aligned with those of the standard PDF card (No. 00-06-0246, Cubic, F-43m). The result indicates that thermal evaporation deposition leads to high-orientation (111) facet CuI thin film. Figure 4a demonstrates the photograph of as-prepared CsCu₂I₃-CuI heterojunction photodetector. As shown in Figure 4b, the linear current–voltage (I - V) curves under dark and illuminations are recorded, and the nonlinear characteristics of the curves indicate the existence of interfacial energy barrier under dark and illuminations. Figure 4c describes the semilogarithmic

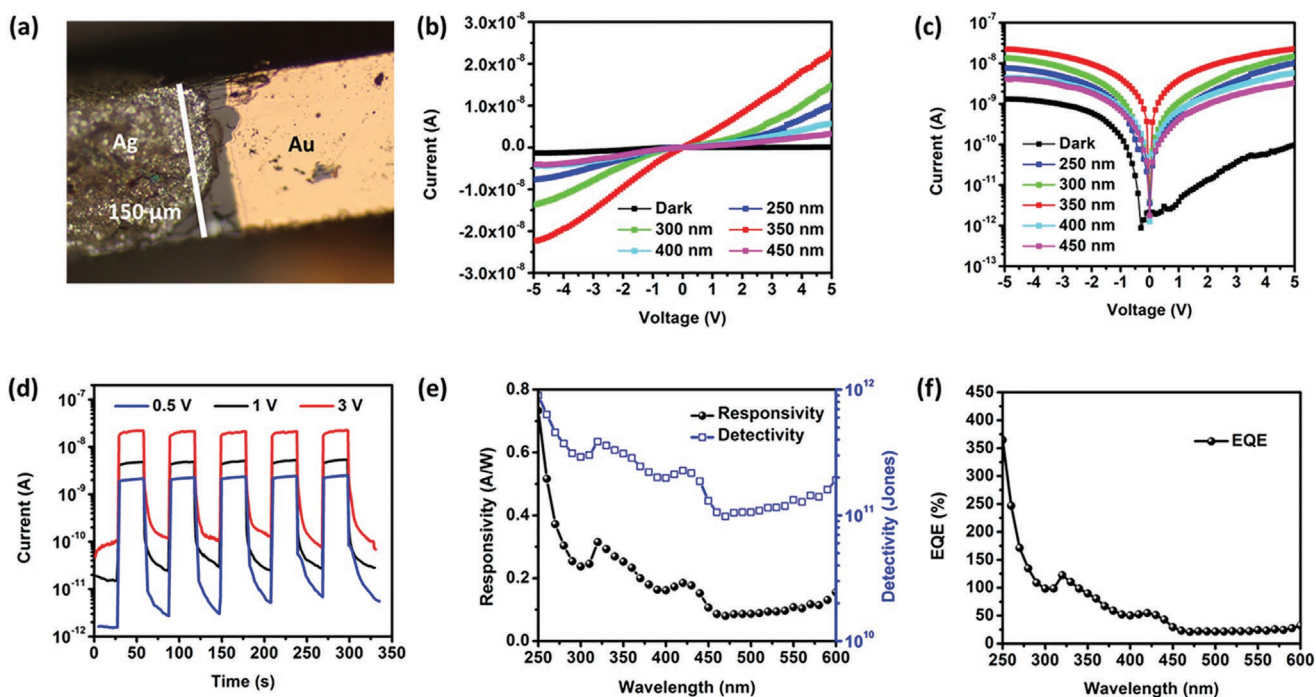


Figure 4. Photoelectric performance of the CsCu₂I₃-CuI heterojunction photodetector. a) Photograph of the device. b) Linear I - V curves under dark and illumination. c) Semilogarithmic I - V curves under dark and illumination. d) Semilogarithmic I - t curves under 350 nm illumination and at different bias voltages. e) Estimated responsivity and specific detectivity curves as a function of wavelength at 3 V bias voltage. f) Estimated EQE curve as a function of wavelength at 3 V bias voltage.

I - V curves of CsCu₂I₃-CuI heterojunction photodetector. It is noted that the dark current curve shows an obvious rectification, and the rectification ratio is as high as at least an order of magnitude. The switch ratio is much higher at forward bias than that at reverse bias, with the value up to 280. Furthermore, the asymmetric Ag and Au electrodes are selected to increase the self-powered performance of the CsCu₂I₃-based photodetector, as depicted in Figure S4 in the Supporting Information. Figure 4d demonstrates semilogarithmic current-time (I - t) curves under 350 nm illumination and at different bias voltages. At 3 V bias voltage, although the switch ratio is low, this device yields a high photocurrent of 20 nA under 350 nm illumination. All on-off cycles under different bias voltages show steady and repeatable dynamic photoresponse. Figure 4e,f describes the responsivity, specific detectivity (D^*) and EQE of this heterojunction photodetector, based on the following equations^[5]

$$R_{\lambda} = \frac{I_{ph} - I_{dark}}{P_{\lambda} S} \quad (4)$$

$$D^* = \frac{R_{\lambda}}{(2eI_{dark}/S)^{1/2}} \quad (5)$$

$$EQE = \frac{hc R_{\lambda}}{e \lambda} \quad (6)$$

considering the photocurrent, dark current and effective illumination area (S) of the photodetector with illumination

wavelength (λ) and light power density (P_{λ}). Under 350 nm illumination and 3 V bias voltage, this device shows a responsivity of 253 mA W⁻¹, which is five times that of previous work.^[7] Moreover, the specific detectivity and EQE are enhanced to 3.1×10^{11} Jones and 90%, respectively, which are greater than those of most reported lead-free halide perovskite analogue photodetectors.^[4]

Bulk single crystal provides high-quality platform to study the intrinsic performance, however, the difficulty to obtain large enough external dimensions limits the construction of electrodes and the growth of ordered patterned structures.^[30] In addition, 1D CsCu₂I₃ demonstrates the advantage of 1D growth, due to the intrinsic 1D crystal structure.^[7] Therefore, space-confined method is adopted to reduce the thickness for potential large-area device fabrication.^[31] According to this point, for the first time, ultralong single-crystalline CsCu₂I₃ microbelt is successfully grown based on the optimized growth strategy. Figure 5a demonstrates the schematic diagram of space-confined growth process, including the hydrophobic treatment, supersaturated droplet, seeding and growing (details in the Experimental Section). Figure 5b shows the optical photographs of the CsCu₂I₃ microbelt with length up to 3.5 mm and aspect ratio up to 600. The width of the CsCu₂I₃ microbelt is adjusted from 6 to 60 μ m. Figure 5c demonstrates the device fabrication process through sequential thermal evaporation deposition of p-CuI, Ag, and Au electrodes using shadow mask. The XRD pattern of the as-grown CsCu₂I₃ microbelt is provided in Figure 5d, which shows a good alignment of most

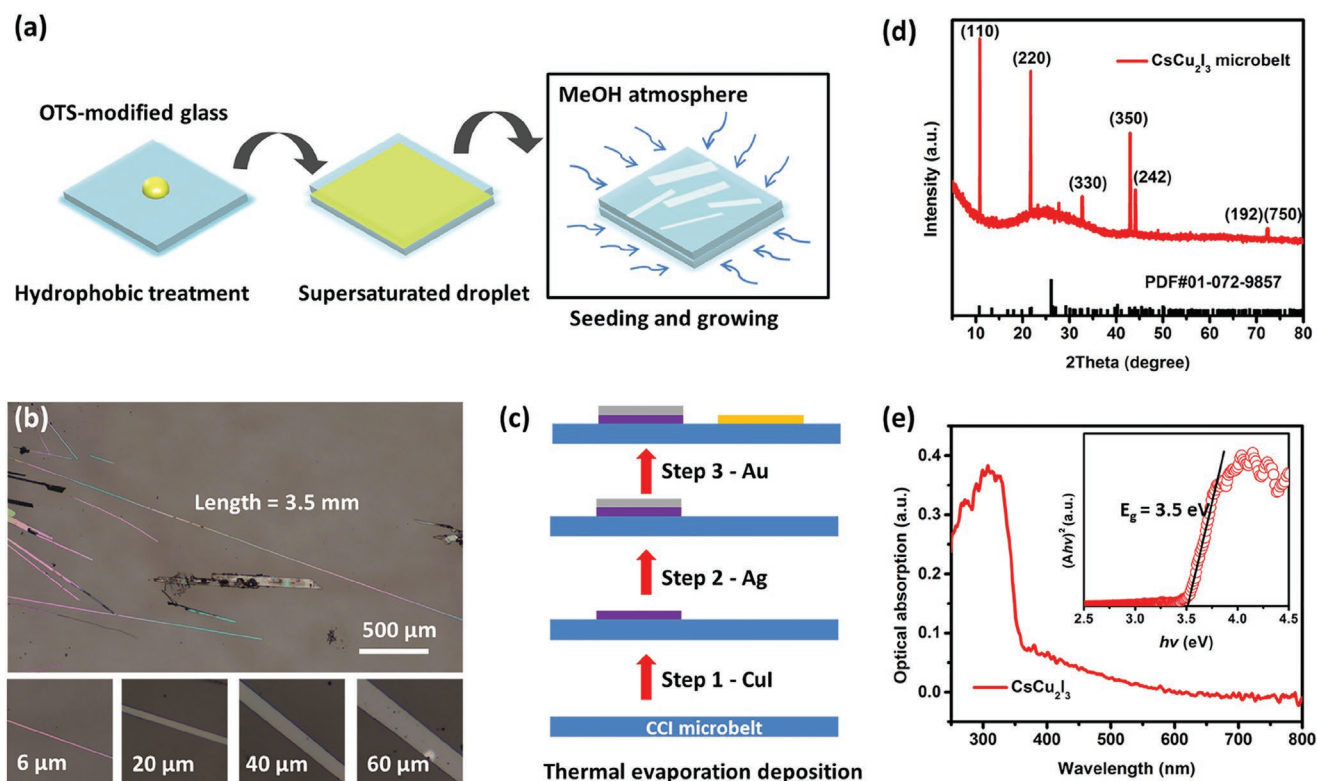


Figure 5. Space-confined growth of ultralong single-crystalline CsCu₂I₃ microbelt and device fabrication. a) Schematic diagram of the space-confined growth process. b) Optical photographs of the CsCu₂I₃ microbelt with different width. c) Thermal evaporation deposition process of p-CuI and electrodes. d) X-ray diffraction pattern of the as-grown CsCu₂I₃ microbelt. e) Optical absorption spectra of CsCu₂I₃ microbelt.

{110} diffraction peaks with the standard card of orthorhombic CsCu_2I_3 (PDF#01-072-9857, Cmc m). Figure 5e demonstrates optical absorption spectra of CsCu_2I_3 microbelt, and this material shows obvious absorption in UV region. The wide bandgap is calculated to be 3.5 eV, which is slightly smaller than CsCu_2I_3 nanowire.

Photoelectric performance of the heterojunction UV photodetector, based on ultralong single-crystalline CsCu_2I_3 microbelt, is systematically studied. Figure 6a demonstrates the photograph of the as-prepared UV photodetector. As shown in Figure S5a,b in the Supporting Information, the switch ratio of the individual CsCu_2I_3 microbelt photodetector is as low as 5 at forward and reverse bias voltage of 3 V, due to the high dark current. The photoresponse stability of CsCu_2I_3 microbelt with symmetric Au electrodes is confirmed by the $I-t$ tests in

Figure S9 in the Supporting Information, due to the high air stability of both CsCu_2I_3 microbelt and Au electrode. After a month, the fact that the dark current gradually increased with the repeated on/off operations is ascribed to surface adsorption or photothermal effect, and this phenomenon can be reduced by decreasing surface defect density.^[32] The CsCu_2I_3 microbelt-based photodetector with asymmetric electrodes shows poor photoresponse stability due to the poor air stability of Ag electrode. Through constructing heterojunction with p-CuI, the heterojunction UV photodetector demonstrates an obviously enhanced switch ratio of 100, owing to suppressed dark current at reverse bias voltage, as shown in Figure 6b. Specifically, the dark current of this heterojunction UV photodetector is reduced by 300 times at -3 V, compared with that of individual CsCu_2I_3 microbelt photodetector. It is also worth noting that the

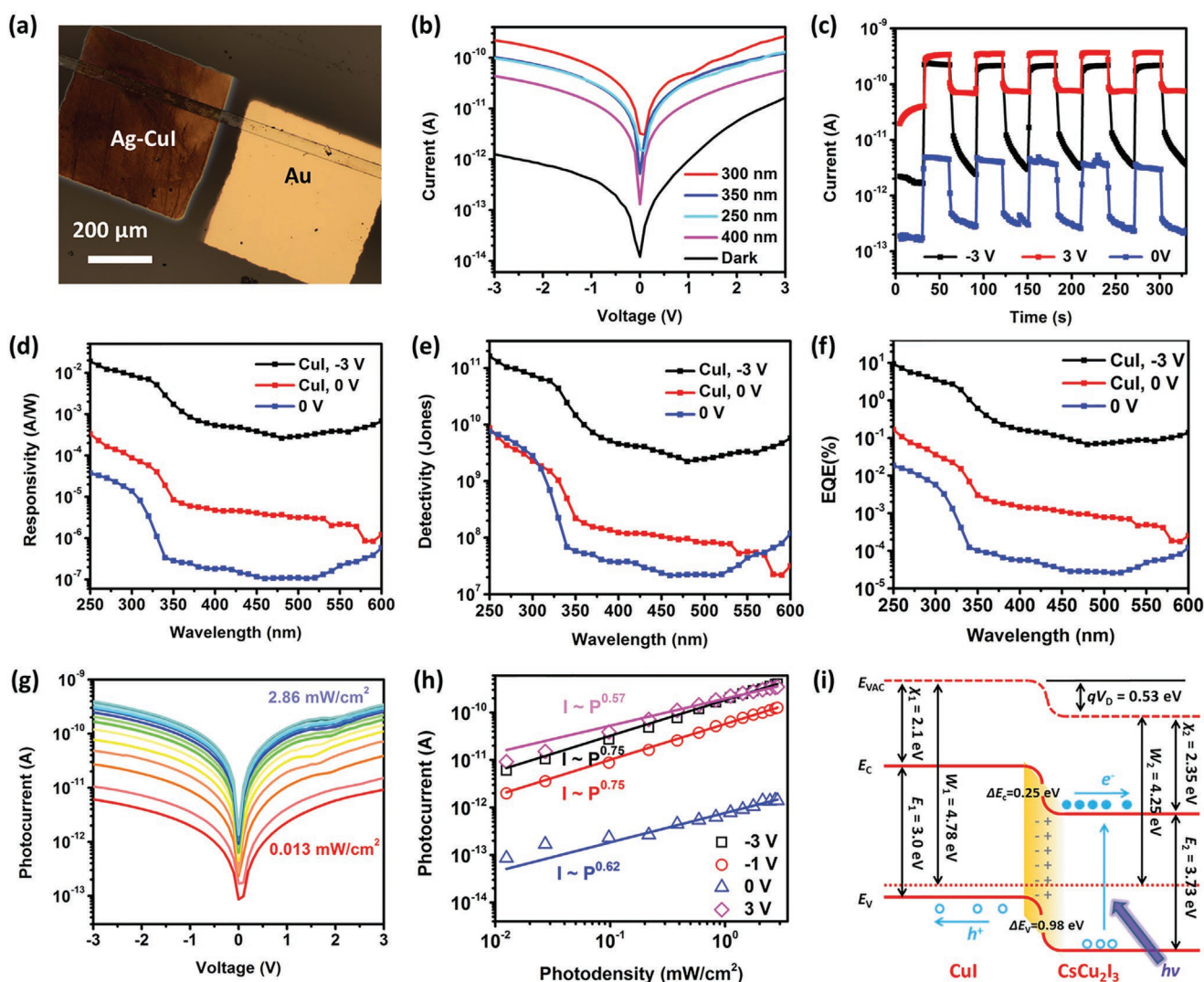


Figure 6. Photoelectric performance of the heterojunction UV photodetector based on ultralong single-crystalline CsCu_2I_3 microbelt. a) Photograph of the device. b) Semilogarithmic I - V curves under dark and illumination. c) Semilogarithmic I - t curves under 300 nm illumination and at different bias voltages. d) Comparison of the estimated responsivity between CsCu_2I_3 microbelt with and without p-CuI. e) Comparison of the estimated detectivity between CsCu_2I_3 microbelt with and without p-CuI. f) Comparison of the estimated EQE between CsCu_2I_3 microbelt with and without p-CuI. g) Light intensity-dependent I - V curves under 300 nm illumination. h) Photocurrent as a function of photodensity and the corresponding power law fitting curves at different bias voltages. i) Band alignment between CsCu_2I_3 and p-CuI.

Table 2. Photoelectric performances of UV photodetectors based on ternary copper iodide and other typical semiconductors.

Material	Photodetector	Light [nm]	P [mW cm ⁻²]	Bias [V]	Responsivity [mA W ⁻¹]	Detectivity [Jones]	Response time rise/decay [ms]	Switch ratio	Rejection ratio	Refs.
Single crystal	Ag–CsCu ₂ I ₃ –Ag	350	0.6	3	126	6.4E+11	0.04/1.6	600	5	This work
	Ag–CsCu ₂ I ₃ /CuI–Au	350	0.6	3	253	3.1E+11	–	280		
	Ag–CsCu ₂ I ₃ –Ag	350	0.6	3	51	9.20E+10	0.25/20	31.5	3	[7]
	Ni–CsCu ₂ I ₃ –Ni	340	3.29	–5	–	–	50.4/244.8	4	4	[11]
Nanobelt	Au/Cr–ZnS–Au/Cr	320	–	20	–	–	2.57/1.99	–	100	[36]
Nanowire	Au–Zn ₂ SnO ₄ –Au	254	–	20	–	–	460/420	–	–	[37]
Microbelt	Au–CsCu ₂ I ₃ –Au	300	0.6	0	0.014	2.5E+9	–	20	206	This work
	Au–CsCu ₂ I ₃ /CuI–Ag	300	0.6	–3	8.8	7.7E+10	–	100	36	
Polycrystalline film	Au–CsCu ₂ I ₃ –Au	265	0.305	3	22.1	1.2E+11	–	22	9	[10]
	Ag–BiOCl–Ag	350	–	5	0.00076	–	1030/10 600	1.7	20	[38]
	Au–MgZnO–Au	350	–	1	0.59	2.7E+6	30 900/39 700	–	400	[39]
	Au–CsPb ₂ Br ₃ –Au	254	–	2	0.24	1E+10	260/280	1000	2	[40]
	CsPbBr ₃ /perovskite photodiode	279	–	–0.1	1.4	2.4E+11	70/70	–	–	[41]
	Au–BeZnO–Au	325	–	5	25	4E+9	1.48/4	–	50	[42]
	Au/Cr–Zn ₂ GeO ₄ –Au/Cr	254	–	20	–	–	300/200	–	3	[43]

peak photoresponse of CsCu₂I₃ microbelt (300 nm) shows an obvious blue-shift than that of CsCu₂I₃ single crystal (350 nm). Figure 6c displays the semilogarithmic I - t curves under 300 nm illumination and at different bias voltages. All photoresponse show stable and repeatable cycles, and the on-off ratio at the bias voltage of –3 V is much greater than that at the bias voltage of 3 V, due to the heterojunction-induced rectification effect. When removing the bias voltage, this device still shows self-powered performance at least an order of magnitude.

To clearly display the sensitivity between these CsCu₂I₃ microbelt-based photodetectors, the responsivity, detectivity, and EQE are calculated and compared, as shown in Figure 6d–f. The UV–vis rejection ratio (R_{250}/R_{400}) is 206 for individual CsCu₂I₃ microbelt photodetector, which indicate good spectral selectivity in UV region for CsCu₂I₃ microbelt. At the bias voltage of 0 V, the device sensitivity is obviously enhanced when combining CsCu₂I₃ and p-CuI. Upon 300 nm illumination, the heterojunction photodetector shows the responsivity of 8.8 mA W⁻¹ and detectivity of 7.7×10^{10} Jones, which are comparable to those of most lead-free halide perovskite analogue photodetectors.^[4] **Table 2** summarizes the key photoelectric parameters for ternary copper iodide based UV photodetectors. It is worth mentioning that the sensitivity of the device drops sharply near 330 nm, which corresponds well to the bandgap of CsCu₂I₃ microbelt single crystal. As shown in Figure 6g, when changing the light power density (300 nm illumination) from 13 to 2.86 mW cm⁻², the photoresponse increases accordingly at different bias voltages. Figure 6h demonstrates the photocurrent as a function of photodensity and the corresponding power law fitting curves at different bias voltages. Under different light power density, the photocurrent obeys the power law relation $I \sim P^\theta$, where θ is at the range of 0.57–0.75. This nonunity power law index is associated to the complex process of the generation, capture, transfer, and recombination of electrons and holes in the photoresponse process for the CsCu₂I₃ microbelt-based photodetector.^[33] The

photodensity-dependent photoresponse reveals the existence of various shallow and deep traps with different energy levels in the bandgap. The higher value θ of 0.75 at reverse bias voltage of –3 V indicates better photoelectric conversion efficiency than that at forward bias voltage of 3 V, and this result is corresponding to higher switch ratio and lower dark current at reverse bias voltage of 3 V. As shown in Figure S5c in the Supporting Information, a higher value θ of 0.77 is obtained in pure CsCu₂I₃ microbelt photodetector, which may be attributed to less interface loss of photogenerated carriers.

Figure 6i describes the typical type-II band alignment of CsCu₂I₃–CuI heterojunction to explain the boosted photoelectric performance of CsCu₂I₃ microbelt. The electron affinity, work function and bandgap of CsCu₂I₃ and CuI are collected from reported literatures.^[9,34] Under UV illumination, the photogenerated electrons and holes will be effectively separated by the built-in electric field without an external power supply, with the total band bending as high as 0.53 eV.^[35] It is noted that the conduction band offset of 0.25 eV promotes the transfer of photogenerated electrons from CuI side to CsCu₂I₃ side, while the valence band offset of 0.98 eV facilitates the transfer of photogenerated holes from CsCu₂I₃ side to CuI side. Therefore, it can be inferred that constructing heterojunction is an effective way to boost the photoelectric performance of the low-dimensional single-crystalline CsCu₂I₃ microbelt. Moreover, the built-in electric field at the CsCu₂I₃–CuI interface is capable of reducing the electron–hole recombination and preventing the electron transport from CsCu₂I₃ to CuI, favoring a low reverse dark current and thus improving the detectivity.

3. Conclusion

As raw material ratio between CuI and CsI changes, the ultimate crystal phase evolves between CsCu₂I₃ and Cs₃Cu₂I₅

single crystals. The photoelectric performances of transparent and colorless CsCu₂I₃ millimeter rod single crystal, including switch ratio and response speed, are successfully boosted by at least one order of magnitude through optimized growth process. The optimized strategy includes room-temperature and selected raw material ratios, which suppress carrier recombination, thus the optimized-grown CsCu₂I₃ single crystals exhibit relatively longer carrier lifetime. Furthermore, the heterojunction UV photodetector based on CsCu₂I₃ millimeter rod single crystal shows a responsivity of 253 mA W⁻¹, a detectivity of 3.1 × 10¹¹ Jones and a EQE of 90%, which are obviously enhanced compared with those in previous work. Moreover, space-confined method is adopted to reduce the thickness of the CsCu₂I₃ single crystal, and therefore CsCu₂I₃ microbelt is obtained to facilitate the device fabrication. The ultralong CsCu₂I₃ microbelt exhibits the length up to 3.5 mm and the aspect ratio up to 600, with the adjustable width from 6 μm to 60 μm. It is worth noting that the dark current of the heterojunction UV photodetector is reduced by 300 times at reverse bias voltage, compared with that of individual CsCu₂I₃ microbelt photodetector. The enhanced performance is derived from superior type-II band alignment between CsCu₂I₃ and CuI, which effectively promotes the separation of photogenerated carrier. This work provides a strategy of growth optimization and device fabrication of low-dimensional halide perovskite analogue for potential application in patterning technology.

4. Experimental Section

Optimized Growth CsCu₂I₃ and Cs₃Cu₂I₅ Single Crystals: CsCu₂I₃ and Cs₃Cu₂I₅ single crystals were grown by antisolvent vapor assisted method at RT. The raw materials CsI (Aladdin Chemistry Co., Ltd., 99.9%), CuI (Aladdin Chemistry Co., Ltd., 99.5%), dimethyl sulfoxide (J&K Scientific Ltd., DMSO, 99.7%), and *N,N*-dimethylformamide (J&K Scientific Ltd., DMF, 99.8%) were used during the growth process. The CsI content was fixed at 2 mmol, and the CuI content was selected to make the raw material ratio ([CuI]/([CuI] + [CsI])) change from 20% to 80%. The CsI and CuI were evenly mixed and dissolved in 2 mL solvent mixture (DMSO: DMF = 1:4), and the mixture was stirred at RT for 2–3 h. Later, anhydrous methanol (Sinopharm Chemical Reagent Co., Ltd., 99.5%) was dropwise added into the mixture until the precipitation did not disappear. The mixture was filtered by filter and syringe to obtain clear precursor saturated solution. Finally, the precursor saturated solution was transferred to the large container full of volatile methanol. After growing at RT for 2–3 days, the as-grown single crystals were obtained and rinsed by isopropanol.

Growth of CsCu₂I₃ Microbelt Single Crystal: Acetone, water, ethanol were used to clean the glass substrates. The mixed solvent of hexane and OTS (Octadecyltrichlorosilane, Sinopharm Chemical Reagent Co., Ltd., 95%), with volume ratio of 500:1, were used to make hydrophobic glasses. The precursor saturated solution was dropped on one glass, and it was covered by another glass to produce a thin liquid film. The sandwich structure glasses were transferred to volatile methanol environment. After 2–3 days growth, the as-grown CsCu₂I₃ microbelt single crystals were obtained and rinsed by isopropanol.

Characterization: Power X-ray diffraction pattern was obtained through Bruker D8 Advance X-ray diffractometer equipped with Cu K α radiation ($\lambda = 0.15406$ nm). The powder sample was measured with the scan step of 0.02° and a staying time of 0.1 s. The optical photographs were taken by Olympus optical microscope. The steady-state photoluminescence (PL) spectrum was performed by Horiba Fluorolog-3 instrument. PL measurement at different temperature was conducted using a closed-cycle helium cryostat system (Jannis; CCS-100). The transient PL

spectrum was carried out using a fluorescence lifetime spectrometer with a pulsed nano-LED excitation source. The optical absorption spectra were investigated by UV–vis spectrophotometer (Hitachi, U-3900H).

Photoelectric Measurement: To facilitate CsCu₂I₃ microbelt UV heterojunction photodetector, a sequential deposition was introduced to pattern the p-CuI layer, Ag electrode, and Au electrode using thermal evaporation deposition process. The light source system was a 75 W Xe lamp equipped with a monochromator. The optical power meter (Ophir NOVA II) was utilized to detect the light power density. The semiconductor measurement system (Keithley 4200-SCS) was used to collect the *I*–*V* and *I*–*t* curves. Q-switch Nd:YAG laser (Continuum Electro-Optics, MINILITE II) was adopted to record the transient photoresponse, accompanied with a resistor and an oscilloscope (Tektronix MSO/DPO5000). All photoelectric tests were performed at RT and ambient atmosphere.

Supporting Information

Supporting Information is available from the Wiley Online Library or from the author.

Acknowledgements

The work was supported by National Key R&D Program of China (No. 2017YFA0204600 and 2018YFA0703700), National Natural Science Foundation of China (No. 51872050 and 12061131009), Science and Technology Commission of Shanghai Municipality (No. 21520712600 and 19520744300), and the China Postdoctoral Science Foundation (2020M681165).

Conflict of Interest

The authors declare no conflict of interest.

Data Availability Statement

Research data are not shared.

Keywords

heterojunctions, lead-free halide perovskite analogue, photophysical processes, ultralong microbelts, UV photodetectors

Received: October 27, 2021
Published online: December 13, 2021

- [1] M. Ahmadi, T. Wu, B. Hu, *Adv. Mater.* **2017**, *29*, 1605242.
- [2] Y. Li, Z. Shi, W. Liang, J. Ma, X. Chen, D. Wu, Y. Tian, X. Li, C. Shan, X. S. Fang, *Mater. Horiz.* **2021**, *8*, 1367.
- [3] Z. Ma, Z. Shi, C. Qin, M. Cui, D. Yang, X. Wang, L. Wang, X. Ji, X. Chen, J. Sun, D. Wu, Y. Zhang, X. J. Li, L. Zhang, C. Shan, *ACS Nano* **2020**, *14*, 4475.
- [4] F. Cao, L. Li, *Adv. Funct. Mater.* **2021**, *31*, 2008275.
- [5] H.-P. Wang, S. Li, X. Liu, Z. Shi, X. S. Fang, J.-H. He, *Adv. Mater.* **2021**, *33*, 2003309.
- [6] Y. Li, Z. Zhou, N. Tewari, M. Ng, P. Geng, D. Chen, P. K. Ko, M. Qammar, L. Guo, J. E. Halpert, *Mater. Chem. Front.* **2021**, *5*, 4796.

- [7] Z. Li, Z. Li, Z. Shi, X. S. Fang, *Adv. Funct. Mater.* **2020**, *30*, 2002634.
- [8] M. Zhang, J. Zhu, B. Yang, G. Niu, H. Wu, X. Zhao, L. Yin, T. Jin, X. Liang, J. Tang, *Nano Lett.* **2021**, *21*, 1392.
- [9] Y. Li, Z. Shi, L. Wang, Y. Chen, W. Liang, D. Wu, X. Li, Y. Zhang, C. Shan, X. S. Fang, *Mater. Horiz.* **2020**, *7*, 1613.
- [10] J. Yang, W. Kang, Z. Liu, M. Pi, L.-B. Luo, C. Li, H. Lin, Z. Luo, J. Du, M. Zhou, X. Tang, *J. Phys. Chem. Lett.* **2020**, *11*, 6880.
- [11] X. Mo, T. Li, F. Huang, Z. Li, Y. Zhou, T. Lin, Y. Ouyang, X. Tao, C. Pan, *Nano Energy* **2021**, *81*, 105570.
- [12] R. Lin, Q. Guo, Q. Zhu, Y. Zhu, W. Zheng, F. Huang, *Adv. Mater.* **2019**, *31*, 1905079.
- [13] B. Xie, R. Xie, K. Zhang, Q. Yin, Z. Hu, G. Yu, F. Huang, Y. Cao, *Nat. Commun.* **2020**, *11*, 2871.
- [14] X. Han, W. Wu, H. Chen, D. Peng, L. Qiu, P. Yan, C. Pan, *Adv. Funct. Mater.* **2021**, *31*, 2005230.
- [15] Y. Tong, B. J. Bohn, E. Bladt, K. Wang, P. Müller-Buschbaum, S. Bals, A. S. Urban, L. Polavarapu, J. Feldmann, *Angew. Chem., Int. Ed.* **2017**, *56*, 13887.
- [16] Y. Chen, G. Chen, Z. Zhou, X. Li, P. Ma, L. Li, W. Yin, H. Zeng, G. Zou, *Adv. Funct. Mater.* **2021**, *n/a*, 2101966.
- [17] P. K. Nayak, D. T. Moore, B. Wenger, S. Nayak, A. A. Haghighirad, A. Fineberg, N. K. Noel, O. G. Reid, G. Rumbles, P. Kukura, K. A. Vincent, H. J. Snaith, *Nat. Commun.* **2016**, *7*, 13303.
- [18] T. J. Savenije, C. S. Ponceca, L. Kunneman, M. Abdellah, K. Zheng, Y. Tian, Q. Zhu, S. E. Canton, I. G. Scheblykin, T. Pullerits, A. Yartsev, V. Sundström, *J. Phys. Chem. Lett.* **2014**, *5*, 2189.
- [19] S. Hull, P. Berastegui, *J. Solid State Chem.* **2004**, *177*, 3156.
- [20] H. Chen, J. M. Pina, F. Yuan, A. Johnston, D. Ma, B. Chen, Z. Li, A. Dumont, X. Li, Y. Liu, S. Hoogland, Z. Zajacz, Z. Lu, E. H. Sargent, *J. Phys. Chem. Lett.* **2020**, *11*, 4326.
- [21] J. R. Lakowicz, *Principles of Fluorescence Spectroscopy*, 3rd ed., Springer, Maryland **2010**.
- [22] H. Song, Y. Lin, M. Zhou, H. Rao, Z. Pan, X. Zhong, *Angew. Chem., Int. Ed.* **2021**, *60*, 6137.
- [23] S. Pathak, A. Sepe, A. Sadhanala, F. Deschler, A. Haghighirad, N. Sakai, K. C. Goedel, S. D. Stranks, N. Noel, M. Price, S. Hüttner, N. A. Hawkins, R. H. Friend, U. Steiner, H. J. Snaith, *ACS Nano* **2015**, *9*, 2311.
- [24] L. Wang, Z. Shi, Z. Ma, D. Yang, F. Zhang, X. Ji, M. Wang, X. Chen, G. Na, S. Chen, D. Wu, Y. Zhang, X. Li, L. Zhang, C. Shan, *Nano Lett.* **2020**, *20*, 3568.
- [25] R. Lin, Q. Zhu, Q. Guo, Y. Zhu, W. Zheng, F. Huang, *J. Phys. Chem. C* **2020**, *124*, 20469.
- [26] T. Jun, T. Handa, K. Sim, S. Iimura, M. Sasase, J. Kim, Y. Kanemitsu, H. Hosono, *APL Mater.* **2019**, *7*, 111113.
- [27] S. Cheng, M. Nikl, A. Beitlerova, R. Kucerkova, X. Du, G. Niu, Y. Jia, J. Tang, G. Ren, Y. Wu, *Adv. Opt. Mater.* **2021**, *n/a*, 2100460.
- [28] T. Jun, K. Sim, S. Iimura, M. Sasase, H. Kamioka, J. Kim, H. Hosono, *Adv. Mater.* **2018**, *30*, 1804547.
- [29] Y. Zhang, S. Li, W. Yang, M. K. Joshi, X. S. Fang, *J. Phys. Chem. Lett.* **2019**, *10*, 2400.
- [30] S.-M. Kim, D.-Y. Khang, *Small* **2014**, *10*, 3761.
- [31] P. Gui, H. Zhou, F. Yao, Z. Song, B. Li, G. Fang, *Small* **2019**, *15*, 1902618.
- [32] D. You, C. Xu, W. Zhang, J. Zhao, F. Qin, Z. Shi, *Nano Energy* **2019**, *62*, 310.
- [33] R. Saran, R. J. Curry, *Small* **2018**, *14*, 1703624.
- [34] D.-K. Ko, P. R. Brown, M. G. Bawendi, V. Bulović, *Adv. Mater.* **2014**, *26*, 4845.
- [35] G. Xing, B. Wu, S. Chen, J. Chua, N. Yantara, S. Mhaisalkar, N. Mathews, T. C. Sum, *Small* **2015**, *11*, 3606.
- [36] X. S. Fang, Y. Bando, M. Liao, T. Zhai, U. K. Gautam, L. Li, Y. Koide, D. Golberg, *Adv. Funct. Mater.* **2010**, *20*, 500.
- [37] Y. Zhang, J. Wang, H. Zhu, H. Li, L. Jiang, C. Shu, W. Hu, C. Wang, *J. Mater. Chem.* **2010**, *20*, 9858.
- [38] W. Ouyang, L. Su, X. S. Fang, *Small* **2018**, *14*, 1801611.
- [39] S.-J. Young, Y.-H. Liu, *Sens. Actuators, A* **2018**, *269*, 363.
- [40] T. Zhang, F. Wang, P. Zhang, Y. Wang, H. Chen, J. Li, J. Wu, L. Chen, Z. D. Chen, S. Li, *Nanoscale* **2019**, *11*, 2871.
- [41] T. Zou, X. Liu, R. Qiu, Y. Wang, S. Huang, C. Liu, Q. Dai, H. Zhou, *Adv. Opt. Mater.* **2019**, *7*, 1801812.
- [42] L. Su, Y. Zhu, X. Xu, H. Chen, Z. Tang, X. S. Fang, *J. Mater. Chem. C* **2018**, *6*, 7776.
- [43] C. Yan, N. Singh, P. S. Lee, *Appl. Phys. Lett.* **2010**, *96*, 053108.